Understanding the re-entrant phase transition in a non-magnetic scheelite.

Matilde Saura-Múzquiz,[a†] Frederick Marlton,[a†] Bryce Mullens,[a] Alicia María Manjón-Sanz,[b] Joerg C. Neuefeind,[b] Michelle Everett,[b] Helen E. A. Brand,[c] S. Mondal[d], G. Vaitheeswaran[e] and Brendan J. Kennedy[a]

[a] *School of Chemistry, University of Sydney, F11, Sydney, NSW 2006, Australia*

[b] *Neutron Scattering Division, Oak Ridge National Laboratory, Oak Ridge, Tennessee 37831 United States*

[c] *Australian Synchrotron, Australian Nuclear Science and Technology Organisation, 800 Blackburn Road, Clayton, Victoria 3168, Australia*

[d] *Advanced Centre of Research in High Energy Materials (ACRHEM), University of Hyderabad, Prof. C. R. Rao Road, Gachibowli, Hyderabad 500046, Telangana, India*

[e] *School of Physics, University of Hyderabad, Prof. C. R. Rao Road, Gachibowli, Hyderabad, 500046, Telangana, India*

† *Equally contributing authors*

Abstract

The stereochemical activity of lone pair electrons plays a central role in determining the structural and electronic properties of both chemically simple materials such as H_2O, as well as more complex condensed phases such as photocatalysts or thermoelectrics. $TlReO_4$ is a rare example of a non-magnetic material exhibiting a re-entrant phase transition and emphanitic behavior in the long-range structure. Here, we describe the role of the Tl^+ $6s^2$ lone pair electrons in these unusual phase transitions and illustrate its tunability by chemical doping, which has broad implications for functional materials containing lone pair bearing cations. First-principles density functional calculations clearly show the contribution of the Tl^+ $6s^2$ in the valence band region. Local structure analysis, *via* neutron total scattering, revealed that changes in the long-range structure of $TlReO_4$ occur due to changes in the correlation length of the Tl^+ lone pairs. This has a significant effect on the anion interactions, with long-range ordered lone pairs creating a more densely packed structure. This resulted in a trade-off between anionic repulsions and lone pair correlations that lead to symmetry lowering upon heating in the long-range structure, whereby lattice expansion was necessary for the Tl^+ lone pairs to become highly correlated. Similarly, introducing lattice expansion through chemical pressure allowed long-range lone pair correlations to occur over a wider temperature range, demonstrating a method for tuning the energy landscape of lone pair containing functional materials.

Keywords

Scheelite, disorder, PDF, phase transition, cation order, lone pair

Introduction

Metal ions containing s^2 lone pair electrons are important for a wide range of functional oxide materials. This is particularly the case in high performance Pb-based ferroelectrics, where it is well established that the $6s^2$ lone pair of the Pb^{2+} cation plays a significant role[1-4]. Despite the continual debate over the exact mechanisms[5], it is accepted that the electron density of the lone pair creates a distortion of the unit cell through correlated Pb displacements, influencing the net electric polarization[6]. Given this, much of the quest for Pb-free ferroelectrics has focused on using the non-toxic and isoelectronic lone pair bearing cation Bi^{3+}.[6,7]

Ferroelectric materials are well known to undergo changes in long-range symmetry with temperature. This is typically from a centrosymmetric high-temperature phase to a non-centrosymmetric low-temperature phase (or sequence of phases) with spontaneous polarization[8,9], and occurs irrespective of the presence of lone pair-bearing metals[10]. In some of these materials, local structure probes have revealed that the cation displacements characteristic of the low symmetry structure persist above the phase transition, but these are disordered and average out crystallographically at high temperature to a high-symmetry structure[11-13]. These disordered displacements are emergent from the low-temperature phase.

Recently, there have been observations in some thermoelectric materials of a high temperature disordered phase with local cation displacements that arise from a low-temperature high-symmetry phase. For example, in the high performance thermoelectric PbTe, the local structure undergoes symmetry lowering upon warming[14], which is in contradiction to ferroelectrics that attain symmetry lowering upon cooling. This phenomenon is very rare among high-symmetry systems and has been called *emphanisis*[14,15], meaning the appearance of a low-symmetry state from a high-symmetry state on warming by virtue of a well-defined displacement of atoms from their centrosymmetric positions. Emphanisis is believed to occur due to a crossover, whereby the lone pairs transition from a stereochemically inactive state at low temperature, to an active state at high temperature due to thermal lattice expansion[14,15].

Emphanitic behavior has been observed in the metal oxide compound $TlReO_4$[16,17], which adopts a scheelite-type structure at high temperature. Scheelites are a family of compounds with the general chemical formula ABO_4 that can accommodate cations with a large variety of ionic radii and oxidation states, from A^{I} and B^{VII} in $KReO_4$ to A^{IV} and B^{IV} in $ZrGeO_4$. The scheelite-type structure is made up of AO_8 and BO_4 polyhedra and its compositional flexibility results in a diverse range of physical and electronic properties. Scheelite-type oxides, such as $CaWO_4$, $BiVO_4$, $KOsO_4$, and $NaLa(MoO_4)_2$, have been extensively studied for technologically-relevant properties including luminescence, ferroelectricity, magnetism, ionic conductivity and photocatalytic activity[18-20].

$TlReO_4$ adopts a low-symmetry monoclinic average structure at room temperature, described in space group $P2_1/c$ (Figure 1a,c). Upon cooling, the macroscopic symmetry of the structure is ***raised*** to the tetragonal $I4_1/a$ (Figure 1b,d) below 160 K. This is distinct from PbTe, which only showed symmetry lowering upon warming in the *local* structure (< 10 Å)[14]. Additionally, a re-entrant phase transition to the tetragonal $I4_1/a$ structure occurs in $TlReO_4$ upon heating

above 450 K. This behavior appears to be unique to $TlReO_4$ and is not observed in the closely-related oxide,$TlTcO_4$ [21]. Although rare, re-entrant phase transitions are occasionally observed in magnetic materials, where ordering of magnetic spins leads to a distortion in the lattice, driving the re-entrant behaviour[22,23]. However, $TlReO_4$ is non-polar and non-magnetic, making this phase transition more unusual. There have been suggestions that the phase transitions in $TlReO_4$ are associated with a charge transfer from $Tl^{I}Re^{VII}O_4$ to $Tl^{III}Re^{V}O_4$, but there is no definitive evidence to support this[24]. Given the presence of an emphanitic phase transition near 160 K, it is more likely that the transitions observed in $TlReO_4$ are associated with a change in the correlations of the $6s^2$ lone pair electrons.

Understanding uncorrelated lone pair distortions requires probes that can extract information on the local scale[14]. Atomic pair distribution function (PDF) analysis is a powerful technique for understanding local-scale distortions[25-27]. The PDF is obtained *via* the Fourier transform of X-ray or neutron total scattering data and corresponds to histograms of interatomic correlations. Total scattering data contains both the Bragg and diffuse signals, meaning the PDF represents local structural information, in addition to the long-range average structure. The advantage of neutron PDF (NPDF) is that it contains detailed information regarding the cation-oxygen bond lengths, which is essential in understanding local-scale cation displacements in metal oxides. In this study, NPDF was used to determine the local-scale structure of $TlReO_4$ for each of the three long-range average structures: low temperature tetragonal, room temperature monoclinic and high temperature tetragonal.

Additionally, two compositional series were studied to further understand the role of the Tl^+ lone pair. This was done by mapping out the phase diagram of $Tl_{1-x}M_xReO_4$ (where M = Rb, Cs), using high-resolution synchrotron X-ray powder diffraction (SXRD). Both Cs^+ and Rb^+ lack the $6s^2$ lone pair, however, Cs^+ has a significantly larger ionic radius (IR) than Tl^+ (1.74 Å vs. 1.59 Å when 8-coordinate), while Rb^+ has a similar IR (1.61 Å)[28]. This also allows for the effect of chemical pressure to be observed in the structure.

In this study we were able to understand the influence of the lone pair in the unusual phase transitions of $TlReO_4$. This is important for expanding current understandings of lone pair bearing metals in the wide range of functional oxide materials.

Experimental methods and Computational details

Sample preparation

Caution! Thallium carbonate is fatal if swallowed, in contact with skin or if inhaled. Appropriate personal protective equipment (PPE) and safe work procedures were employed during sample preparation and sample manipulation.

21 polycrystalline samples with compositions $Tl_{1-x}M_xReO_4$, where M = Rb/Cs and x = 0.0–1.0 in steps of 0.1, were prepared using a co-precipitation method by reacting perrhenic acid with the corresponding carbonate. A 0.2 M solution of rhenium metal in 30% H_2O_2 was prepared and left stirring overnight to form perrhenic acid. Aqueous solutions of Tl_2CO_3 (0.1 M), Rb_2CO_3 (1.5 M) and Cs_2CO_3 (1.5 M) were prepared by dissolving each compound (Sigma Aldrich, Technical grade) in deionized water. The corresponding volume of carbonate solutions were mixed

(*i.e.* $Tl_2CO_{3(aq)}$ + $Rb_2CO_{3(aq)}$ or $Tl_2CO_{3(aq)}$ + $Cs_2CO_{3(aq)}$), and each carbonate mix was poured into the corresponding amount of $HReO_4$ solution, which led to the formation of a white precipitate. The supernatant was discarded, and the precipitate was dried overnight in an oven at 120°C. The powders were then annealed in a furnace at 550°C for 72 hours to obtain the final product. Powder X-ray diffraction was used to confirm the sample purity and crystallinity.

Characterization

Neutron scattering data were collected on $TlReO_4$ using the Nanoscale Ordered MAterials Diffractometer (NOMAD)[29] and POWGEN diffractometer[30] at the Spallation Neutron Source (SNS) located at Oak Ridge National Laboratory (ORNL). The sample was loaded into an 8 mm vanadium can. Diffraction data collected on POWGEN for Rietveld and PDF analysis were collected with a center wavelength of 1.5 and 0.8 Å, respectively[30]. For the PDF calculation, the neutron scattering data were corrected for instrument background, the incident neutron spectrum, absorption and multiple scattering, and finally normalized. The software PDFgetN3 was used to calculate the PDF from the POWGEN data[31]. For PDFs derived from NOMAD data, a Fourier filter was applied to the S(Q) for Q > 16 $Å^{-1}$ to reduce the noise in the broad regions of the reciprocal space data (Figure S1). For data collected on NOMAD and POWGEN, a Q_{max} of 46 and 39 $Å^{-1}$, respectively was used for the PDF calculation.

Synchrotron X-ray diffraction data were measured on the Powder Diffractometer BL-10 at the Australian Synchrotron using 21.0 keV photons (λ = 0.589056 Å). Rietveld Refinement of LaB_6 (NIST SRM660B) standard was used to determine the Thompson Cox Hastings instrument resolution function[32]. Data were measured using an array of 16 Mythen II microstrip detector modules. To eliminate the gap between individual modules two data sets were collected with the detector assembly shifted by 0.5°. Each sample was placed in a 0.2 mm quartz capillary that was rotated during the measurement to minimize preferred orientation effects. Temperature control was achieved using an Oxford Cryosystems Cryostream. Structural refinements against the powder diffraction data and PDF data were conducted using the software TOPAS[33]. The first-principles calculations were performed using the full potential linearized augmented plane wave (FP-LAPW) method as implemented in WIEN2K code[34]. Generalized Gradient Approximation (GGA) functional PBE[35] has been considered to incorporate the exchange-correlation energy. The separation between the core and valence electrons was restricted to -7 Ry. A value of $RK_{max} = 7$ was used for obtaining the proper basis set and the number of k-points was set to 500 to carry out these calculations.

Results

The two different long-range structures of $TlReO_4$ are illustrated in Figure 1a-d, and additional structural figures with alternative projections are in Figure S2-5. The corresponding neutron powder diffraction data for these structures at 20, 300 and 500 K are shown in Figure 2 and Figure S6-7. Rietveld refinements using the structural models in Figure 1a-d show excellent agreement with the experimental neutron powder diffraction data. In the tetragonal ($I4_1/a$) structure, three crystallographically distinct sites are occupied, corresponding to a Tl, Re and O site, where only the *x*, *y*, and *z* coordinates of the O site are not constrained by symmetry and can be refined. In the monoclinic structure ($P2_1/c$), the degrees of freedom are much larger, with three sites for each of the Tl and Re cations and twelve oxygen sites, all of which have variable *x*, *y*, and *z* fractional coordinates. In the monoclinic structure, the ReO_4 tetrahedra are rotationally distorted (Figure 1a) due to the presence of the Tl^+ $6s^2$ lone pair, which also distorts the TlO_8

polyhedra (Figure 1c) and results in a large distribution of Tl-O bond lengths (Figure 1e). In the tetragonal structure, the ReO_4 tetrahedra are highly ordered (Figure 1b), resulting in two distinct Tl-O bond lengths (Figure 1e). There are no distortions in the tetragonal structure to account for the presence of the lone pair of the Tl^+ cation, which would indicate the lone pair is stereochemically inactive in the high- and low-temperature tetragonal phases.

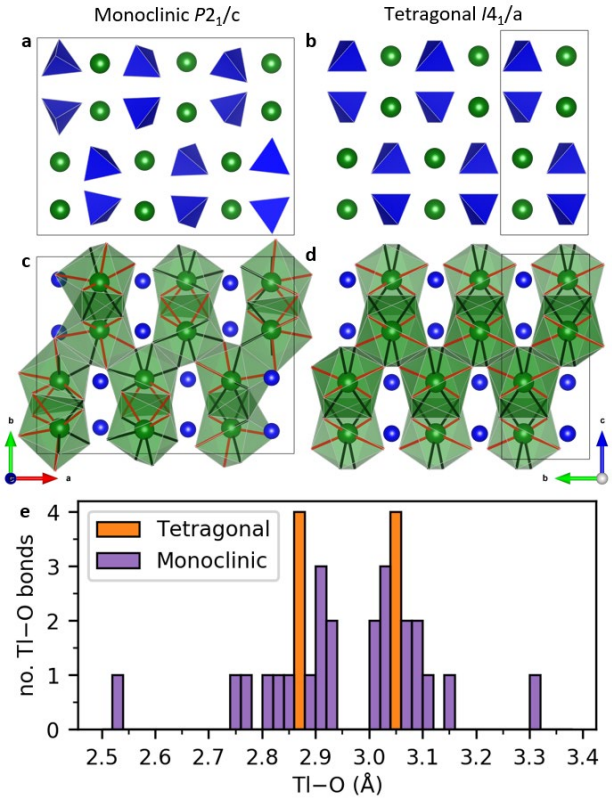

Figure 1. The monoclinic (**a,c**) and tetragonal (**b,d**) structures of $TlReO_4$ along the *c* and *a* axes, respectively. **e** Histogram (bin width = 0.02 Å) of the unique Tl-O bond lengths for the two structures within the unit cell. **a,b** illustrate the rotational distortion of the rigid ReO_4 tetrahedra (blue), while **c,d** illustrate the distortions of the TlO_8 polyhedra (green). The red and black lines in **c,d** correspond to Tl-O bond lengths that are longer and shorter than 2.975 Å, respectively.

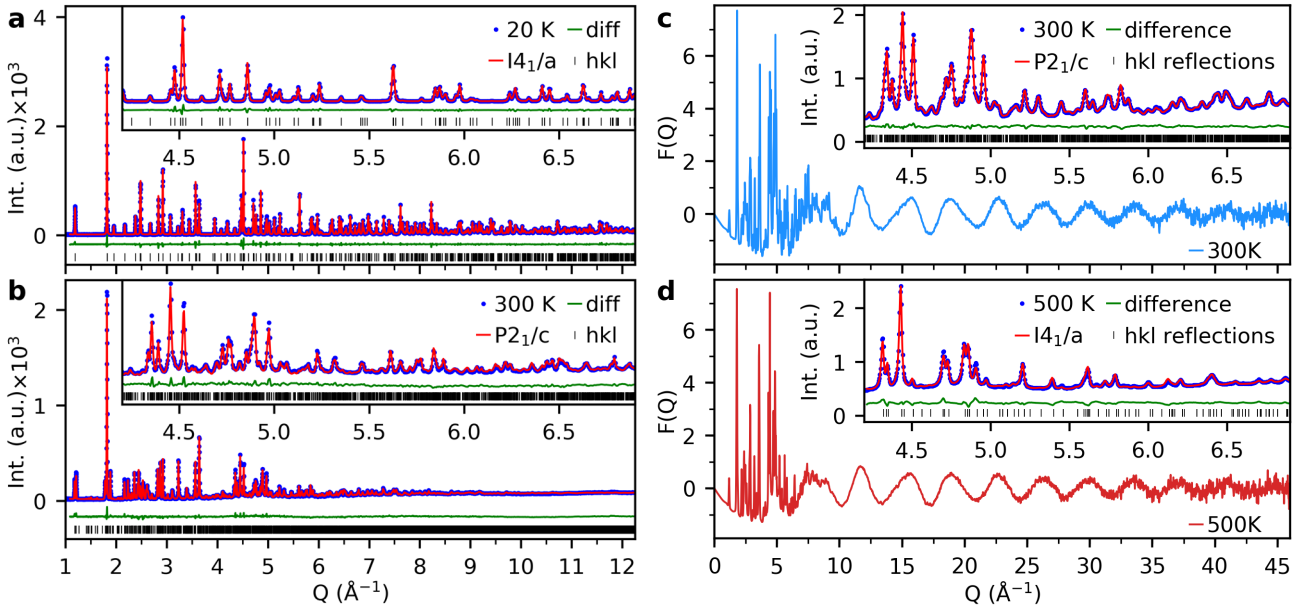

Figure 2. (**a,b**) Neutron powder diffraction data and Rietveld refinement at 20 and 300 K on $TlReO_4$. Data was collected on the POWGEN instrument at ORNL, λ = 1.5 Å. (**c,d**) Neutron total scattering data F(Q) = Q[S(Q) – 1][25]

at 300 and 500 K on $TlReO_4$, collected on NOMAD instrument at ORNL. Insets in **c,d** show Rietveld refinements from the high resolution back scattering bank of the NOMAD instrument[29].

To further investigate the behavior of the average structure of $TlReO_4$ with respect to temperature, X-ray powder diffraction (XPD) data were measured and analyzed across 100–475 K in increments of 5 K. The most notable property obtained from the Rietveld refinements of this data was the relatively large change in the volume of the unit cell (Figure 3). For comparison between the different structures, the volume of the tetragonal cell was multiplied by 3. Upon heating, the volume of the $TlReO_4$ unit cell decreases significantly in the transition to the monoclinic structure. Further heating caused the unit cell to transition back to the tetragonal structure at high temperatures with another significant increase in the volume. This indicates that the distortions of the monoclinic structure result in a more closely packed arrangement of the ions, despite the presence of a stereochemically active Tl^+ lone pair. The tetragonal and monoclinic structures co-existed over a relatively narrow temperature range, 135-170 K and 380-390 K, symptomatic of a first order phase transition.

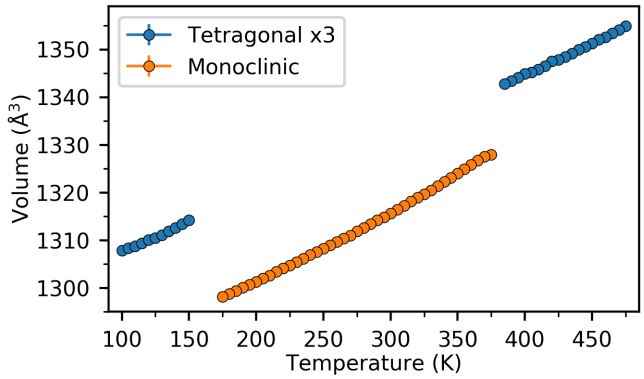

Figure 3. Unit cell volume *vs* Temperature for the single phase regions of $TlReO_4$ across 100–475 K.

Neutron total scattering data were measured at 20, 300, and 500 K to understand the local structure in each of the average structure phases of $TlReO_4$. Although the low-temperature tetragonal phase occurs below about 160 K, measuring at 20 K significantly reduces thermal motion to more clearly reveal static disorder[36]. The neutron F(Q) of $TlReO_4$ at 300 K and 500 K over 0–45 Å^{-1} is shown in Figure 2c,d, where broad wave-like features in the intensity are observed for $5 \leq Q \leq 45$ Å^{-1}, which indicates a mixture of order and disorder in the structure.

The NPDF data of $TlReO_4$ at 20, 300, and 500 K is shown in Figure 4. For each of these temperatures, fits were conducted using both the tetragonal and monoclinic structural models across $1.0 \leq r \leq 30.0$ Å. The first narrow peak in all the NPDF, that occurs at ~ 1.73 Å, corresponds to the 1st Re-O pair, *i.e.* that of the ReO_4 tetrahedra. This peak shows no splitting at any of the measured temperatures, which confirms the presence of rigid ReO_4 tetrahedra. Hence, fitting with both the tetragonal and monoclinic models was conducted with the Re and O atoms constrained to form rigid tetrahedra and prevent any unphysical distortions. Given the rigid nature of the ReO_4 tetrahedra, the first O-O distance, which corresponds to the edge of the tetrahedra, shows a consistent peak at ~ 2.80 Å. The remaining peaks between $2.5 \leq r \leq 3.5$ Å correspond to a mixture of the nearest neighbor Tl-O and subsequent O-O pairs. Further Tl-O and O-O pairs continue to influence the PDF for $3.5 \leq r \leq 5.0$ Å. However, there are also prominent features due to the presence of the 2nd Re-O pair at ~ 3.6 Å, the 1st Tl-Tl pair at ~ 4.1 Å and all cation-cation pairs at ~ 4.35 Å.

The fits at 20 K (Figure 4a,b) show that the monoclinic model produces a better fit than the tetragonal model. This is most noticeable for $2.5 \leq r \leq 3.5$ Å, indicating that the local structure contains Tl-O and O-O distortions that cannot be accounted for in the tetragonal model, despite it being a good description of the long-range average structure. In the 300 K NPDF data (Figure 4c,d), the monoclinic and tetragonal models produce different quality fits. This is not only noticed across the local-scale features, but across the whole fit, which clearly indicates that both the local and average structures are best described by the monoclinic unit cell. At 500 K (Figure 4e,f), the monoclinic structure still provides a better fit to the data, but in this case, the biggest differences are noticed for $r < 5$ Å. Similar to the low-temperature tetragonal structure, the high-temperature structure has local distortions that deviate away from the average tetragonal structure. In both the 300 and 500 K data, the tetragonal model fits the first Re-O peak ($r \sim 1.73$ Å) poorly. This is not because the tetragonal model poorly describes the Re-O distance but rather it is due to a larger oxygen atomic displacement parameter (ADP) occurring, that broadens the peaks across 2.5–3.5 Å in order to minimize the residual curve in the least squares process. This, in turn, creates a broader Re-O peak than is observed experimentally. This broadening is not necessary in the monoclinic fits and hence the 1st Re-O peak is fit better with a more appropriate ADP. The fits to the NPDF data show that even though the average structure at low/high temperature is tetragonal, there are short-range distortions, most obvious for $2.5 \leq r \leq 5.0$ Å, that are better described using the monoclinic unit cell. This is because the monoclinic unit cell allows for distortions of the TlO_8 polyhedra through the rotations of the ReO_4 tetrahedra (Figure 1a,c). The presence of locally distorted TlO_8 polyhedra within the long-range tetragonal structure indicates that the Tl^+ lone pairs are stereochemically active, but not sufficiently correlated for the long-range monoclinic structure to form.

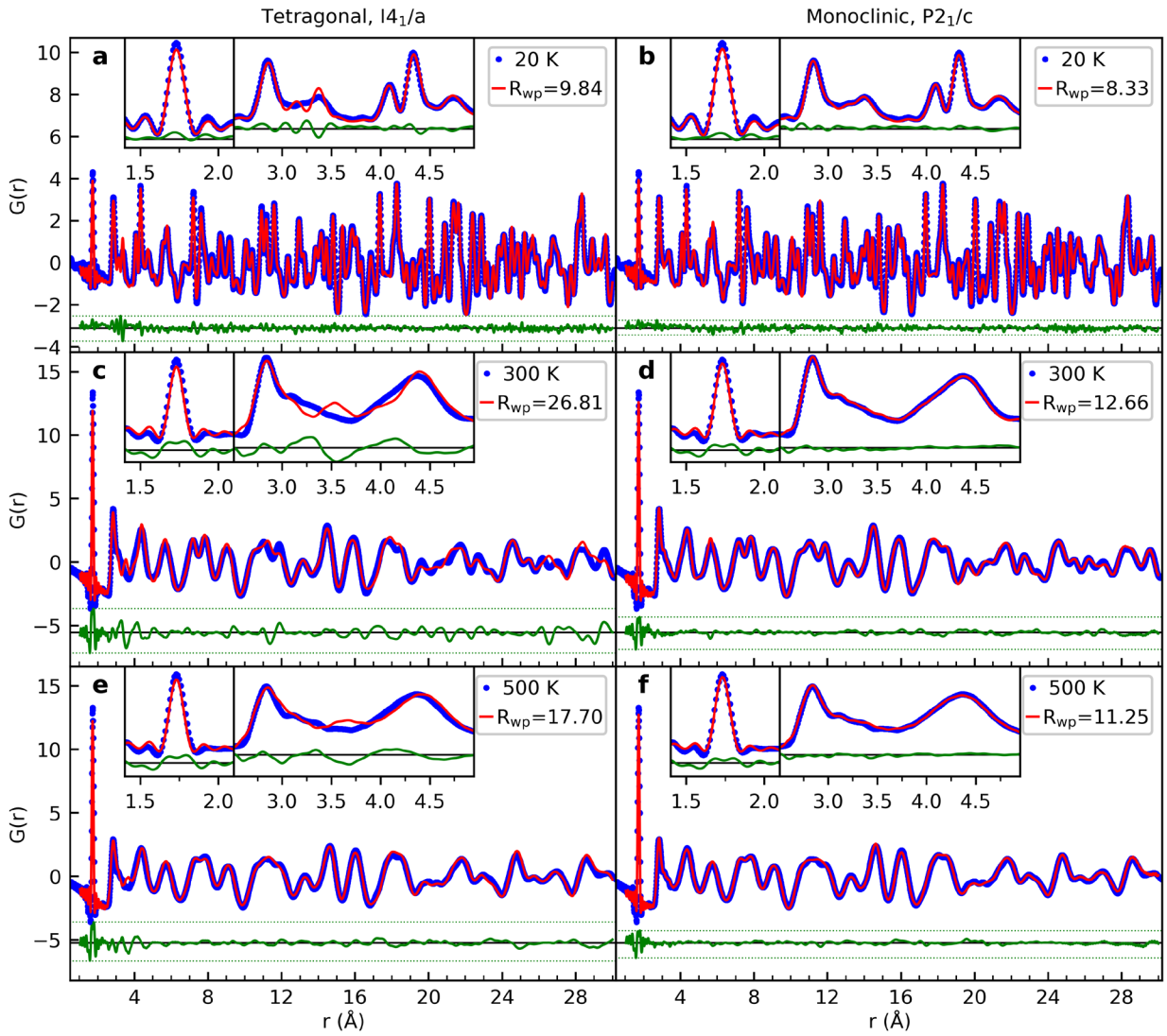

Figure 4: NPDF data analysis of $TlReO_4$ collected at 20 (a,b), 300 (c,d) and 500 K (e, f). Fits were conducted for $1.0 \leq r \leq 30.0$ Å using the tetragonal structure (left column, a,c,e) and the monoclinic structure (right column, b, d, f) at each temperature. The data at 20 K were measured on POWGEN ($\lambda = 0.8$ Å), whilst the remaining data were measured using NOMAD ($0.2 \leq \lambda \leq 3.0$ Å) at ORNL. The blue dots correspond to the measured data, whilst the red and green lines are the fit and difference, respectively. Insets at the top of each plot show the PDF peaks for $1.4 \leq r \leq 2.1$ Å and $2.51 \leq r \leq 4.95$ Å.

To further understand the role of the lone pair distortions in the structure of $TlReO_4$, chemical substitution experiments were conducted with cations lacking lone pair electrons and of differing ionic radius (IR). The two different strategies investigated were the replacement of the Tl^+ ion (IR = 1.59 Å) with the much larger Cs^+ (IR = 1.74 Å) and with comparably sized Rb^+ (IR = 1.61 Å). In both cases, the substitution removes the lone pair of Tl^+, but will have different effects on the structure due to differences in the IR.

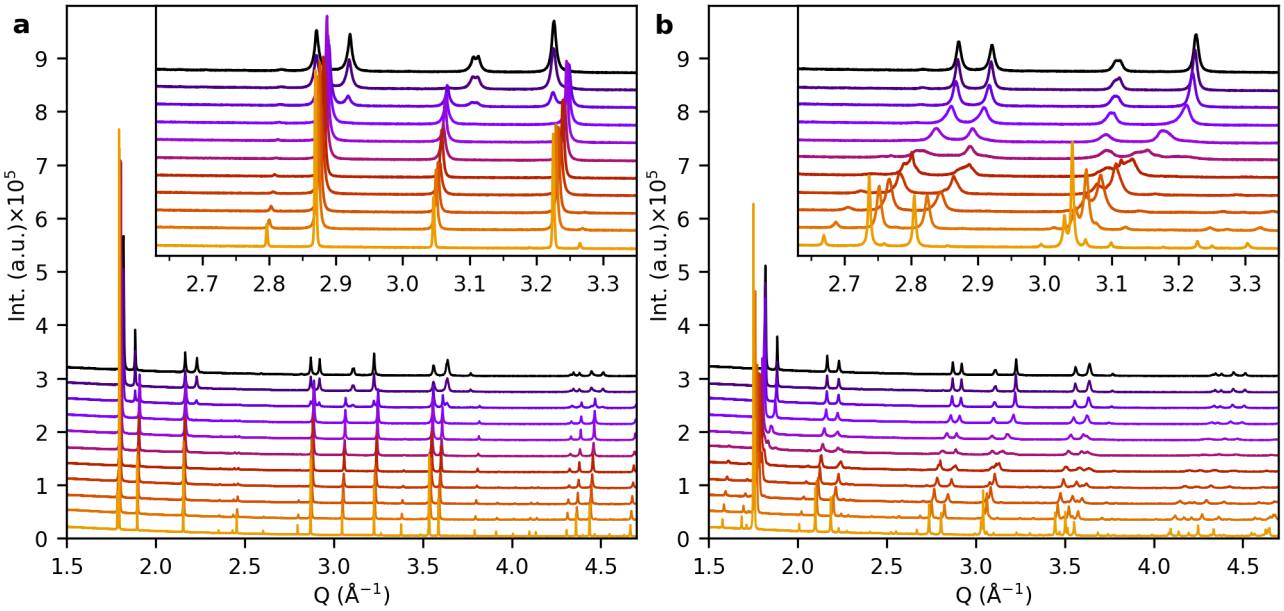

Figure 5: SXRD data at 300 K for $Tl_{1-x}M_xReO_4$, where M = Rb in **a** and M = Cs in **b**. The top darkest trace corresponds to x = 0.0, with increments of 0.1 for subsequent plots until the bottom lightest trace with x = 1.0.

SXRD data at 300 K for the two compositional series $Tl_{1-x}M_xReO_4$ (M = Cs, Rb) are shown in Figure 5, while data at 95 and 480 K are shown in Figure S8-11. Rietveld refinements against each of the end-member compositions from Figure 5 are shown in Figure 6, confirming single-phase samples. As described in our previous works, at room temperature $CsReO_4$ adopts an orthorhombic (*Pnma*) pseudo-scheelite structure and $RbReO_4$ has the archetypical tetragonal ($I4_1/a$) scheelite structure[16].

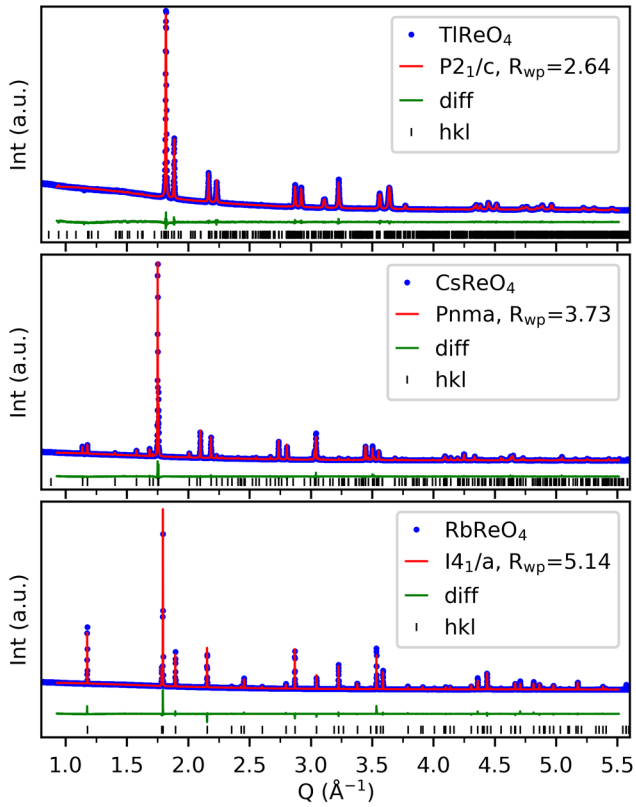

Figure 6: Rietveld refinements against the SXRD data for each of the end-member compositions in $Tl_{1-x}M_xReO_4$ (M = Cs, Rb) at 300 K.

For M = Rb at 300 K (Figure 5a), the monoclinic structure is maintained for a small range of $0 \leq x \leq 0.1$. At $x = 0.2$ a mixed phase is observed and for $x \geq 0.3$ the single phase tetragonal ($I4_1/a$) structure forms. Across the series there is a small shift in peak positions to lower Q, which corresponds to the slight expansion of the unit cell due to the slightly larger Rb^+. In the compositional series with M = Cs at 300 K (Figure 5b), the monoclinic structure is maintained for a larger range of $0 \leq x \leq 0.4$, which is confirmed by the Rietveld refinements in Figure S12-15. Across the $Tl_{1-x}Cs_xReO_4$ series, there is a much larger shift in the peak positions to lower Q due to the incorporation of the much larger Cs^+. The strain created due to chemical pressure (*i.e.* partially replacing the small Tl^+ with a larger Cs^+ cation) can be observed from the broadening of the Bragg peaks in the monoclinic phase for $0.1 \leq x \leq 0.4$ in Figure S16 and is most noticeable for $Tl_{0.6}Cs_{0.4}ReO_4$ (x = 0.4). The results from Rietveld refinements for the monoclinic region with $0.0 \leq x \leq 0.4$ in $Tl_{1-x}Cs_xReO_4$ at 300 K are shown in Figure S17, with the changes in the unit cell volume and β angle shown in Figure 7. With Cs doping, the volume of the unit cell increases substantially and the β angle is reduced to 90°, before the 2-phase mixture occurs at x = 0.5 and x = 0.6 (Figure 5b). For $x \geq 0.7$, a single phase orthorhombic structure is observed[16]. These observations at 300 K are summarized in Figure 8. For both cation substitutions, the monoclinic structure would be disrupted due to the removal of the Tl^+ lone pair. This is evident in the Rb^+ doped series, where small doping levels (x > 0.1) leads to de-stabilization of the monoclinic structure. Unexpectedly, the presence of the relatively large Cs^+ ion maintains the monoclinic structure for larger concentrations than Rb^+.

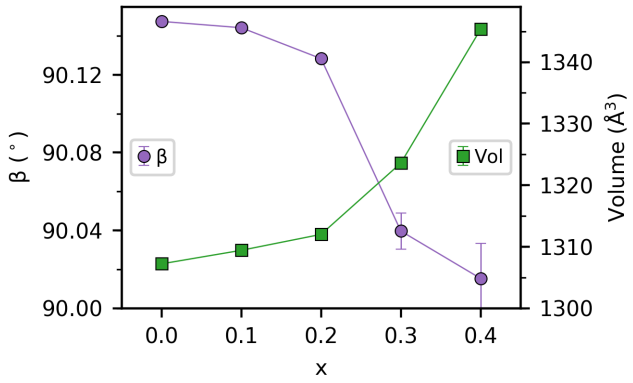

Figure 7: Unit cell volume and lattice angle β in monoclinic $Tl_{1-x}Cs_xReO_4$ for $0.0 \leq x \leq 0.4$ at 300 K

Doping with Cs^+ also influenced the stability of the monoclinic phase with respect to temperature, as outlined in the structural phase diagram of Figure 8. At 95 K, compositions in the Cs series with x = 0.1 are in the tetragonal structure, akin to the undoped $TlReO_4$. However, at x = 0.3 and x = 0.4, a single-phase monoclinic structure is observed, with a mixture of the two phases occurring for x = 0.2. Corresponding Rietveld refinements are shown in Figure S18-19 clearly demonstrating a single-phase monoclinic structure for x = 0.3 and x = 0.4 at 95 K. This was not observed in the $Tl_{1-x}Rb_xReO_4$ series, which exhibited the tetragonal structure for all compositions at 95 K. This indicates that the Cs doping has made the monoclinic structure stable over a wider temperature range compared to the undoped $TlReO_4$, despite the reduced presence of Tl^+ lone pairs suggesting chemical pressure is playing a role. For a few samples, the Bragg reflections in the patterns measured at 95 K were broader than in the corresponding pattern measured at 300 or 480 K. It is believed that this is a consequence of the presence of microstrains introduced as the sample was rapidly (< 1 min) cooled through the monoclinic to tetragonal transition in going from room temperature to 95 K.

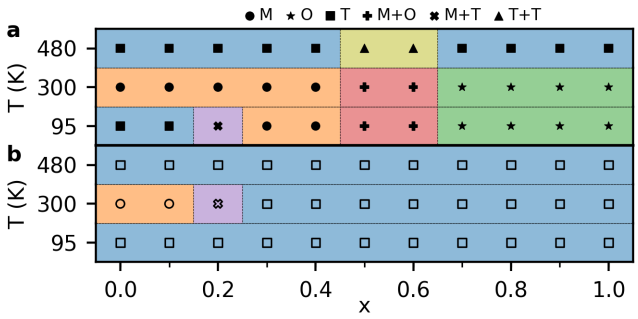

Figure 8: Phase diagram for $Tl_{1-x}M_xReO_4$, where M = Cs in **a** and M = Rb in **b**. Filled and open markers correspond to the Cs and Rb doped series, respectively. The labels M, O and T refer to the monoclinic ($P2_1/c$), orthorhombic (*Pnma*), and tetragonal ($I4_1/a$) structures respectively. Colored shading and dashed lines outline the different phase regions.

To further understand the effects of Cs doping, variable temperature SXRD measurements were conducted on $Tl_{1-x}Cs_xReO_4$ for x = 0.2 and x = 0.4 over 95 – 480 K, as shown in Figure 9. Over this temperature range, $Tl_{0.8}Cs_{0.2}ReO_4$ undergoes a similar re-entrant phase transition, that is observed in the undoped $TlReO_4$, between the tetragonal and monoclinic structures. However, in $Tl_{0.8}Cs_{0.2}ReO_4$, the monoclinic structure is maintained over a wider temperature range (120–387 K) than in undoped $TlReO_4$ (170–380 K). For $Tl_{0.6}Cs_{0.4}ReO_4$ the monoclinic structure persists over a still wider temperature range, with the high temperature transition occurring at 405 K and the low temperature transition not being observed within the measured temperature range. This provides further confirmation that higher concentrations of Cs in $Tl_{1-x}Cs_xReO_4$ stabilizes the monoclinic structure, where it forms, over a wider temperature range despite the reduced concentration of lone pairs and the increased chemical pressure.

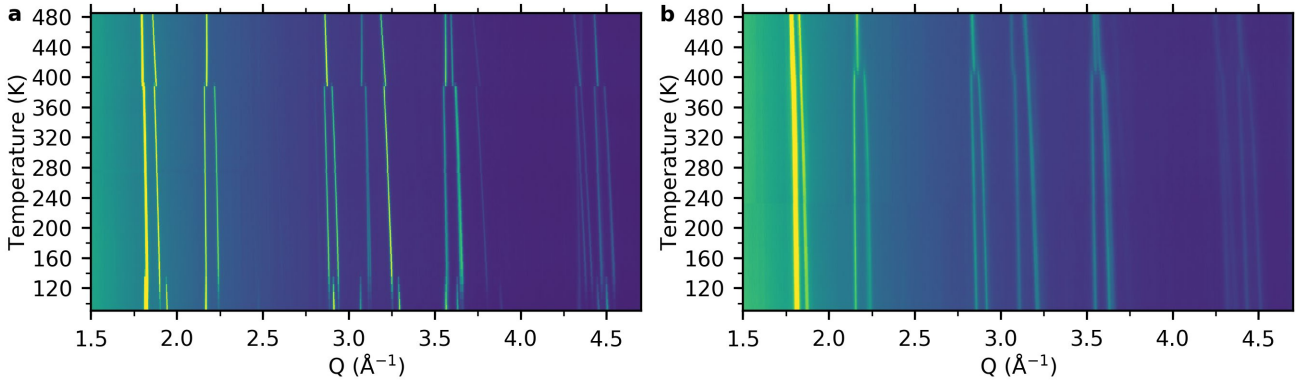

Figure 9: Variable temperature SXRD of $Tl_{0.8}Cs_{0.2}ReO_4$ (**a**) and $Tl_{0.6}Cs_{0.4}ReO_4$ (**b**) over 95–480 K. The intensity of the diffraction patterns corresponds to the brightness. Phase transitions can be observed at 120 and 387 K in $Tl_{0.8}Cs_{0.2}ReO_4$ and 405 K in $Tl_{0.6}Cs_{0.4}ReO_4$.

Rietveld refinements across the variable temperature SXRD data were conducted with the resultant unit cell volume shown in Figure 10a and all other parameters in Figure S20-21. In the undoped $TlReO_4$ there is a sudden increase in the unit cell volume (Figure 3) at the phase boundary between the monoclinic and high-temperature tetragonal structures. This also occurs for the same phase transition in $Tl_{0.8}Cs_{0.2}ReO_4$ and $Tl_{0.6}Cs_{0.4}ReO_4$ and has been labelled ΔV_{MT} in Figure 10a. However, in these compositions ΔV_{MT} appears to be slightly smaller compared to $TlReO_4$. To quantify this, a linear function was fit to the volume *vs* temperature data in Figure 10a and Figure 3 and the difference in volume between the two curves at the phase boundary temperature was calculated. The resultant ΔV_{MT} values for

each composition are displayed in Figure 10b. With the increased content of Cs, the "jump" in the unit cell volume across the phase boundary decreased.

Variable temperature XPD data were also collected on $Tl_{0.9}Rb_{0.1}ReO_4$ (Figure S22), with the refined unit cell volume in Figure S23 and the resultant ΔV_{MT} in Figure 10b. Even with such small levels of Rb doping, the ΔV_{MT} (12.03 $Å^3$) and the phase boundary temperature, T_{PB}, (390 K) have been more significantly impacted compared to the Cs doping. The magnitude of ΔV_{MT} is a result of the change in the ordering of the lone pairs and it follows that this should scale with the concentration of these. Although this expectation is met in Figure 10b, it is observed that the size of the dopant cation (either Rb or Cs) is also important. Partially replacing Tl^+ with Cs^+ increases the chemical pressure in the system and helps stabilize the monoclinic structure, which partially negates the effect of reducing the concentration of lone pairs.

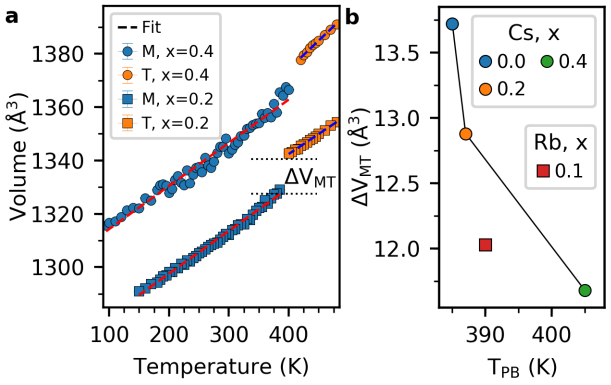

Figure 10: **a** Unit cell volume vs temperature of the single-phase regions of $Tl_{0.8}Cs_{0.2}ReO_4$ and $Tl_{0.6}Cs_{0.4}ReO_4$ over 95–480 K. M and T refer to the monoclinic and tetragonal structures, respectively. The tetragonal volume displayed was multiplied by 3 for comparison with the monoclinic cell. The overlaid dashed lines correspond to a linear fit for the individual phases that is used to calculate ΔV_{MT}. **b** Change in ΔV_{MT} with respect to phase boundary temperature (T_{PB}) for x = 0.0, 0.2 and 0.4 in $Tl_{1-x}Cs_xReO_4$ series, and for x=0.1 in $Tl_{1-x}Rb_xReO_4$ series.

Discussion and Conclusion

Using NPDF we have experimentally shown that $TlReO_4$ exhibits local distortions that are best described by the monoclinic unit cell irrespective of the long-range average structure. Hence, the transitions that occur in the long-range structure are influenced by changes in the correlation length of the Tl^+ lone pairs. The changes in unit cell volume (Figure 3) across the different phases of $TlReO_4$ demonstrate that the ordering of the lone pairs causes the ions in the structure to become more closely packed and indicates that in the formation of the monoclinic structure there is a trade-off between the coherent ordering of the Tl^+ lone pairs and the interatomic distances.

First principle density functional theory (DFT) calculations show that ordering of the Tl $6s^2$ electrons, as occurs in the monoclinic structure, lowers the energy of the system compared to a structure with fully disordered Tl $6s^2$ electrons[37] and, as experimentally observed, this is the favoured long-range structure at room temperature. The energy difference between the two structures is however small (Table S1) Both structures are insulators with large band gaps (Figure S24,25 and Table S1), where the Tl $6s^2$ electrons play a major role in the valance band region[38]. The transition between the monoclinic and tetragonal structures in $TlReO_4$ strongly impacts the anion sublattice, as shown by the

significant differences in the arrangement of the ReO_4 tetrahedra (Figure 1). When heating from the low temperature tetragonal phase, the lattice gradually expands, resulting in increased flexibility towards rotation of the ReO_4 tetrahedra. We propose that at a critical temperature this increased flexibility, due to thermal expansion, facilitates long-range ordering of the Tl $6s^2$ lone pairs and cooperative tilting of the tetrahedra, resulting in the monoclinic structure with increased packing efficiency of the unit cell. The DFT calculations also predicted that the equivalent volume of the monoclinic cell is smaller than that of the tetragonal cell[37]. This symmetry lowering upon heating in the tetragonal-monoclinic transition of $TlReO_4$ is in contradiction to the observations in $RbReO_4$ and perovskite oxides, where increases in temperature reduce the magnitude of cooperative rotations of the polyhedral, ultimately increasing symmetry.

Further heating to the high temperature tetragonal phase increases the thermal motion of the atoms, especially of the lighter oxygen anions, leading to the lone pairs again becoming disordered resulting in a significant expansion of the unit cell. This is commonly referred to as "melting" of the lone pairs by analogy with the melting of ice[39]. This disordering of the lone pair is accompanied by the loss of the complex cooperative tilting of the ReO_4 tetrahedra that is characteristic of the monoclinic structure. In brief, rotation of the ReO_4 tetrahedra in $TlReO_4$ facilitates cooperative ordering of the Tl^+ lone pairs and impacts cation-cation interactions.

Substituting Tl^+ with Rb^+ does not introduce appreciable chemical pressure and has little impact on the unit cell volume of the structure reflecting their similar IR. However, the lack of the lone pair electrons in Rb^+ compared to Tl^+ destabilizes the monoclinic structure at very low doping levels ($x \geq 0.2$). Conversely, adding Cs^+ to the system, which also lacks lone pair electrons, increases the unit cell volume and stabilizes the monoclinic structure over larger doping levels ($x < 0.5$) and over a wider temperature range. It is surprising that substituting the Tl^+ for the significantly larger Cs^+ can stabilise the monoclinic structure as this doping strategy impacts the cation-cation interactions and the ReO_4 tetrahedra much more severely than the Rb^+ doping.

There is the possibility that local Tl-Tl pairs would be "pushed" closer together due to the chemical pressure created by Cs^+. This could increase the strength of the local Tl-Tl interactions compared to the Rb^+ doping, where negligible chemical pressure is created. However, these local Tl-Tl interactions are likely to have a small influence on the structure compared to the average Tl-Tl interactions, which are weaker due to the expansion of the lattice. Overall, doping with Cs^+ weakens the interactions between Tl-Tl pairs due to loss of lone pairs and lattice expansion. Hence, there must be a compensating factor that stabilizes the monoclinic structure.

The doping with Cs^+ will also have an influence on the ReO_4 tetrahedra. This is because the O^{2-} ions between neighboring tetrahedra will be pushed further apart on average and would have a significant impact on the ionic repulsive forces. Experimentally, we observe that highly correlated lone pairs in the monoclinic structure result in shorter O-O distances (excluding the 1st nearest neighbors). The Cs^+ doping increases the distance between anions on average and hence will reduce anionic repulsive forces and increase flexibility for tetrahedral rotation. This additional flexibility compensates for the reduced lone pairs and allows the monoclinic structure, with cooperative tetrahedral rotations and long-range ordered lone pairs, to occur over a wider temperature range before transitioning

into the tetragonal structure. This correlates with the transition between the tetragonal-monoclinic structures in the undoped $TlReO_4$ at 160K, whereby heating influences the flexibility for the formation of the monoclinic structure. With increased doping of Cs^+ ($0.5 \geq x \geq 0.6$), the reduction of Tl^+ lone pairs and increased structural strain no longer makes the monoclinic structure viable, resulting in a mixed phase. In the case of Rb^+ doping, there is insufficient chemical pressure to influence the tetrahedral rotations and counteract the loss of the Tl^+ lone pair. Hence, smaller concentrations of Rb^+ are required to hinder the formation of the monoclinic structure. Although, it is expected that the tetragonal phases of $Tl_{1-x}Rb_xReO_4$ with high concentrations of Tl^+ would exhibit local lone pair distortions away from the average structure akin to the undoped $TlReO_4$.

This study demonstrates the delicate interplay between lone pair correlations, polyhedral rotations, and interatomic distances, and establishes a process whereby the correlation length of lone pairs in a metal oxide can be influenced by the modification of interatomic distances through chemical doping. Specifically, increasing the distance between anions increases the polyhedral rotational flexibility required for the stabilization of lone pair ordering. This illustrates that the correlations between lone pairs are not only influenced by the concentration of lone pair bearing metals, but the overall interaction energy of the entire structure. This is of significance for the broad range of functional materials, such as ferroelectrics or thermoelectrics, where lone pair bearing metals play an important role in the physical properties. The determination of the local distortions in this study is also relevant for the related scheelite structured double tungstate and molybdate crystals[40-45], such as $NaBi(WO_4)_2$. These materials are of interest for laser applications as the large bandwidths associated with the chemical disorder on the *A*-site allow tunability in broad spectral ranges. The disordered nature of these materials make characterization difficult as Raman studies showed additional bands that do not relate to the average structure[41,42]. In our work, we have demonstrated that local structure analysis *via* total scattering is critical in understanding the nature of these local distortions and the behavior of functional materials containing lone pair bearing metals.

Acknowledgements

This work was financially supported by the Australian Research Council and was facilitated by access to Sydney Analytical, a core research facility at the University of Sydney. The work was in part undertaken on the powder diffraction beamline at the Australian Synchrotron. BGM thanks the Australian Institute for Nuclear Science and Engineering for a PGRA scholarship. SM acknowledges DRDO, India, through ACRHEM (DRDO/18/1801/2016/01038: ACRHEM-PHASE-III) for the financial support. GV acknowledges Institute of Eminence University of Hyderabad (UoH-IoE-RC3-21-046) for funding and CMSD University of Hyderabad for providing the computational facility.

References

1 Zhang, N. *et al.* The missing boundary in the phase diagram of $PbZr_{1-x}Ti_xO3$. *Nature Communications* **5**, 5231, doi:10.1038/ncomms6231 (2014).

2 Zhang, N. *et al.* Local-scale structures across the morphotropic phase boundary in PbZr1-xTixO3. *IUCrJ* **5**, 73-81, doi:doi:10.1107/S2052252517016633 (2018).
3 Zhao, C., Li, F., Zhang, S., Li, S. & Jones, J. L. Mechanisms underpinning the ultrahigh piezoelectricity in Sm-doped 0.705Pb(Mg1/3Nb2/3)O3-0.295PbTiO3: Temperature-induced metastable local structure and field-induced polarization rotation. *Journal of Applied Physics* **126**, 075101, doi:10.1063/1.5089477 (2019).
4 Takenaka, H., Grinberg, I., Liu, S. & Rappe, A. M. Slush-like polar structures in single-crystal relaxors. *Nature* **546**, 391-395, doi:10.1038/nature22068 (2017).
5 Cohen, R. E. Relaxors go critical. *Nature* **441**, 941-942, doi:10.1038/441941a (2006).
6 Rödel, J. *et al.* Perspective on the Development of Lead-free Piezoceramics. *Journal of the American Ceramic Society* **92**, 1153-1177, doi:10.1111/j.1551-2916.2009.03061.x (2009).
7 Hong, C.-H. *et al.* Lead-free piezoceramics – Where to move on? *Journal of Materiomics* **2**, 1-24, doi:https://doi.org/10.1016/j.jmat.2015.12.002 (2016).
8 Dragan, D. Ferroelectric, dielectric and piezoelectric properties of ferroelectric thin films and ceramics. *Reports on Progress in Physics* **61**, 1267 (1998).
9 Kwei, G. H., Lawson, A. C., Billinge, S. J. L. & Cheong, S. W. Structures of the ferroelectric phases of barium titanate. *The Journal of Physical Chemistry* **97**, 2368-2377, doi:10.1021/j100112a043 (1993).
10 Jaffe, B., Cook, W. R. & Jaffe, H. L. *Piezoelectric ceramics*. Vol. 3 (Academic Press, 1971).
11 Senn, M. S., Keen, D. A., Lucas, T. C. A., Hriljac, J. A. & Goodwin, A. L. Emergence of Long-Range Order in $BaTiO_3$ from Local Symmetry-Breaking Distortions. *Physical Review Letters* **116**, 207602, doi:10.1103/PhysRevLett.116.207602 (2016).
12 Matsunaga, T., Fons, P., Kolobov, A. V., Tominaga, J. & Yamada, N. The order-disorder transition in GeTe: Views from different length-scales. *Applied Physics Letters* **99**, 231907, doi:10.1063/1.3665067 (2011).
13 Qiu, X., Proffen, T., Mitchell, J. F. & Billinge, S. J. L. Orbital Correlations in the Pseudocubic<mml:math xmlns:mml="http://www.w3.org/1998/Math/MathML" display="inline"><mml:mi>O</mml:mi></mml:math>and Rhombohedral<mml:math xmlns:mml="http://www.w3.org/1998/Math/MathML" display="inline"><mml:mi>R</mml:mi></mml. *Physical Review Letters* **94**, doi:10.1103/physrevlett.94.177203 (2005).
14 Bozin, E. S. *et al.* Entropically Stabilized Local Dipole Formation in Lead Chalcogenides. *Science* **330**, 1660-1663, doi:10.1126/science.1192759 (2010).
15 Knox, K. R., Bozin, E. S., Malliakas, C. D., Kanatzidis, M. G. & Billinge, S. J. L. Local off-centering symmetry breaking in the high-temperature regime of SnTe. *Physical Review B* **89**, doi:10.1103/physrevb.89.014102 (2014).
16 Chay, C. *et al.* Crystal structures and phase transition behaviour in the 5d transition metal oxides $AReO_4$ (A = Ag, Na, K, Rb, Cs and Tl). *Dalton Transactions* **48**, 17524-17532, doi:10.1039/c9dt04021h (2019).
17 Jayaraman, A., Kourouklis, G. A., Fleming, R. M. & Van Uitert, L. G. Temperature-induced phase transitions in $TlReO_4$: A Raman spectroscopic and x-ray diffraction study. *Physical Review B* **37**, 664-667, doi:10.1103/PhysRevB.37.664 (1988).
18 A, M., J, M., Ashokkumar, M. & Arunachalam, P. A review on $BiVO_4$ photocatalyst: Activity enhancement methods for solar photocatalytic applications. *Applied Catalysis A: General* **555**, 47-74, doi:10.1016/j.apcata.2018.02.010 (2018).
19 Yang, C. *et al.* Nano-structured NaLa(MoO4)2 and Eu3+-doped NaLa(MoO4)2: Synthesis, characterizations, photoluminescence and superhydrophobic properties. doi:10.1016/j.mseb.2016.02.002 (2016).
20 Brazdil, J. F. Scheelite: a versatile structural template for selective alkene oxidation catalysts. *Catalysis Science & Technology* **5**, 3452-3458, doi:10.1039/c5cy00387c (2015).

21 Kennedy, B. J., Injac, S., Thorogood, G. J., Brand, H. E. A. & Poineau, F. Structures and Phase Transitions in Pertechnetates. *Inorganic Chemistry* **58**, 10119-10128, doi:10.1021/acs.inorgchem.9b01257 (2019).

22 Scheie, A. *et al.* Reentrant Phase Diagram of $Yb_2Ti_2O_7$ in a ⟨111⟩ Magnetic Field. *Physical Review Letters* **119**, 127201, doi:10.1103/PhysRevLett.119.127201 (2017).

23 Surampalli, A., Egli, R., Prajapat, D., Meneghini, C. & Reddy, V. R. Reentrant phenomenon in the diffuse ferroelectric $BaSn_{015}Ti_{0.85}O_3$: Local structural insights and first-order reversal curves study. *Physical Review B* **104**, 184114, doi:10.1103/PhysRevB.104.184114 (2021).

24 Ablett, J. M., Rueff, J. P., Shieh, S. R., Kao, C. C. & Wang, S. Possible evidence for high-pressure induced charge transfer in thallium rhenium oxide at room temperature. *Physical Review B* **92**, doi:10.1103/physrevb.92.014113 (2015).

25 Terban, M. W. & Billinge, S. J. L. Structural Analysis of Molecular Materials Using the Pair Distribution Function. *Chemical Reviews*, doi:10.1021/acs.chemrev.1c00237 (2021).

26 Christiansen, T. L., Cooper, S. R. & Jensen, K. M. Ø. There's no place like real-space: elucidating size-dependent atomic structure of nanomaterials using pair distribution function analysis. *Nanoscale Advances* **2**, 2234-2254, doi:10.1039/d0na00120a (2020).

27 Playford, H. Y., Owen, L. R., Levin, I. & Tucker, M. G. New Insights into Complex Materials Using Reverse Monte Carlo Modeling. *Annual Review of Materials Research* **44**, 429-449, doi:10.1146/annurev-matsci-071312-121712 (2014).

28 Shannon, R. Revised effective ionic radii and systematic studies of interatomic distances in halides and chalcogenides. *Acta Crystallographica Section A* **32**, 751-767, doi:10.1107/S0567739476001551 (1976).

29 Neuefeind, J., Feygenson, M., Carruth, J., Hoffmann, R. & Chipley, K. K. The Nanoscale Ordered MAterials Diffractometer NOMAD at the Spallation Neutron Source SNS. *Nuclear Instruments and Methods in Physics Research Section B: Beam Interactions with Materials and Atoms* **287**, 68-75, doi:10.1016/j.nimb.2012.05.037 (2012).

30 Huq, A. *et al.* POWGEN: rebuild of a third-generation powder diffractometer at the Spallation Neutron Source. *Journal of Applied Crystallography* **52**, 1189-1201, doi:doi:10.1107/S160057671901121X (2019).

31 Juhás, P., Louwen, J. N., Van Eijck, L., Eelco & Simon. PDFgetN3: atomic pair distribution functions from neutron powder diffraction data using ad hoc corrections. *Journal of Applied Crystallography* **51**, 1492-1497, doi:10.1107/s1600576718010002 (2018).

32 Thompson, P., Cox, D. E. & Hastings, J. B. Rietveld refinement of Debye-Scherrer synchrotron X-ray data from Al2O3. *Journal of Applied Crystallography* **20**, 79-83, doi:doi:10.1107/S0021889887087090 (1987).

33 Coelho, A. TOPAS and TOPAS-Academic: an optimization program integrating computer algebra and crystallographic objects written in C++. *Journal of Applied Crystallography* **51**, 210-218, doi:doi:10.1107/S1600576718000183 (2018).

34 Blaha, P., Schwarz, K., Madsen, G. K., Kvasnicka, D. & Luitz, J. WIEN2K, An Augmented Plane Wave+ Local Orbitals Program for Calculating Crystal Properties, edited by K. *Schwarz, Vienna University of Technology, Austria* (2001).

35 Perdew, J. P., Burke, K. & Ernzerhof, M. Generalized Gradient Approximation Made Simple. *Physical Review Letters* **77**, 3865-3868, doi:10.1103/PhysRevLett.77.3865 (1996).

36 Marlton, F. P. *et al.* Lattice Disorder and Oxygen Migration Pathways in Pyrochlore and Defect-Fluorite Oxides. *Chemistry of Materials* **33**, 1407-1415, doi:10.1021/acs.chemmater.0c04515 (2021).

37 Mondal, S. *et al.* Crystal structure and phase transition of TlReO4: a combined experimental and theoretical study. *Journal of Physics: Condensed Matter* **33**, 065403, doi:10.1088/1361-648x/abb651 (2021).

38 Mukherjee, S., T, A., Mondal, S. & Vaitheeswaran, G. Electronic structure, phonons and optical properties of baryte type scintillators $TlXO_4$ (X = Cl, Br). *Journal of Physics: Condensed Matter* **34**, 115502, doi:10.1088/1361-648x/ac4347 (2022).

39 Shoemaker, D. P. *et al.* Atomic displacements in the charge ice pyrochlore $Bi_2Ti_2O_6O'$ studied by neutron total scattering. *Physical Review B* **81**, 144113, doi:10.1103/PhysRevB.81.144113 (2010).

40 Rico, M. *et al.* Polarization and local disorder effects on the properties of Er^{3+}-doped $XBi(YO_4)_2$, X=Li or Na and Y=W or Mo, crystalline tunable laser hosts. *Journal of the Optical Society of America B* **23**, 2066, doi:10.1364/josab.23.002066 (2006).

41 Maczka, M., Kokanyan, E. P. & Hanuza, J. Vibrational study and lattice dynamics of disordered NaBi(WO4)2. *Journal of Raman Spectroscopy* **36**, 33-38, doi:10.1002/jrs.1263 (2005).

42 Cascales, C., Méndez Blas, A., Rico, M., Volkov, V. & Zaldo, C. The optical spectroscopy of lanthanides R3+ in ABi(XO4)2 (A=Li, Na; X=Mo, W) and LiYb(MoO4)2 multifunctional single crystals: Relationship with the structural local disorder. *Optical Materials* **27**, 1672-1680, doi:10.1016/j.optmat.2004.11.051 (2005).

43 Hideki, K., Naoko, M. & Akihiko, K. Photophysical and Photocatalytic Properties of Molybdates and Tungstates with a Scheelite Structure. *Chemistry Letters* **33**, 1216-1217, doi:10.1246/cl.2004.1216 (2004).

44 Hanuza, J. *et al.* Structure and vibrational properties of tetragonal scheelite NaBi(MoO4)2. *Journal of Raman Spectroscopy* **28**, 953-963, doi:https://doi.org/10.1002/(SICI)1097-4555(199712)28:12<953::AID-JRS190>3.0.CO;2-N (1997).

45 Hanuza, J., Mączka, M. & Van Der Maas, J. H. Polarized IR and Raman spectra of tetragonal NaBi(WO4)2, NaBi(MoO4)2 and LiBi(MoO4)2 single crystals with scheelite structure. *Journal of Molecular Structure* **348**, 349-352, doi:10.1016/0022-2860(95)08660-n (1995).